Contents lists available at ScienceDirect

NeuroImage

Increased sensitivity and signal-to-noise ratio in diffusion-weighted MRI using multi-echo acquisitions

Cornelius Eichner [a,*], Michael Paquette [a], Toralf Mildner [b], Torsten Schlumm [b], Kamilla Pléh [c,d], Liran Samuni [d,e], Catherine Crockford [d,f], Roman M. Wittig [d,f], Carsten Jäger [g,h], Harald E. Möller [b], Angela D. Friederici [a], Alfred Anwander [a]

[a] Max Planck Institute for Human Cognitive and Brain Sciences, Department of Neuropsychology, Leipzig, Germany
[b] Max Planck Institute for Human Cognitive and Brain Sciences, NMR Group, Leipzig, Germany
[c] Robert Koch Institute, Epidemiology of Highly Pathogenic Microorganisms, Berlin, Germany
[d] Taï Chimpanzee Project, Centre Suisse de Recherches Scientifiques, Abidjan, Côte d'Ivoire
[e] Harvard University, Department of Human Evolutionary Biology, Cambridge, MA, United States
[f] Max Planck Institute for Evolutionary Anthropology, Department of Human Behavior, Ecology and Culture, Leipzig, Germany
[g] Paul Flechsig Institute for Brain Research, University of Leipzig, Germany
[h] Max Planck Institute for Human Cognitive and Brain Sciences, Department of Neurophysics, Leipzig, Germany

ARTICLE INFO

ABSTRACT

Post-mortem diffusion MRI (dMRI) enables acquisitions of structural imaging data with otherwise unreachable resolutions - at the expense of longer scanning times. These data are typically acquired using highly segmented image acquisition strategies, thereby resulting in an incomplete signal decay before the MRI encoding continues. Especially in dMRI, with low signal intensities and lengthy contrast encoding, such temporal inefficiency translates into reduced image quality and longer scanning times. This study introduces Multi Echo (ME) acquisitions to dMRI on a human MRI system - a time-efficient approach, which increases SNR (Signal-to-Noise Ratio) and reduces noise bias for dMRI images. The benefit of the introduced ME-dMRI method was validated using numerical Monte Carlo simulations and showcased on a *post-mortem* brain of a wild chimpanzee. The proposed Maximum Likelihood Estimation echo combination results in an optimal SNR without detectable signal bias. The combined strategy comes at a small price in scanning time (here 30% additional) and leads to a substantial SNR increase (here white matter: ~ 1.6x, equivalent to 2.6 averages, grey matter: ~ 1.9x, equivalent to 3.6 averages) and a general reduction of the noise bias.

1. Introduction

Diffusion-weighted MRI (dMRI) is capable of non-invasively probing microstructure and structural connectivity of brain tissue. As a purely structural measure, dMRI can also provide insights into the organization of *post-mortem* brain tissue. Such *post-mortem* dMRI acquisitions allow extremely high image resolutions at the cost of increased scan times (Dyrby et al., 2011; McNab et al., 2013; Miller et al., 2011). Unfortunately, the fixation of the brain in paraformaldehyde solution produces a cross-linkage of proteins which reduces the diffusivity of water molecules in the tissue and the directional contrast (Roebroeck et al., 2019). Hence, to achieve sufficient diffusion contrast, *post-mortem* diffusion-weightings need to be increased relative to *in-vivo* acquisitions.

The vast potential of dMRI in neuroscience and clinical practice led to recent developments of highly specialized human-size MRI systems with very strong diffusion gradients of up to 300 mT/m (Jones et al., 2018; Setsompop et al., 2013). By reducing the echo time of diffusion weighted acquisitions, these novel systems allow advanced dMRI acquisitions with increased signal-to-noise ratio (SNR) and, thus, higher image resolution and stronger diffusion-weightings.

Despite its versatile applications in neuroscience and clinics, dMRI acquisitions and models suffer from various shortcomings. Since the diffusion contrast is realized by direction-weighted signal attenuation, dMRI inevitably suffers from low SNR. This problem is systematically worsened for dMRI acquisitions with increased diffusion-weighting and higher image resolutions. In low SNR regimes (SNR<10), the typically employed magnitude dMRI signals become biased by non-Gaussian
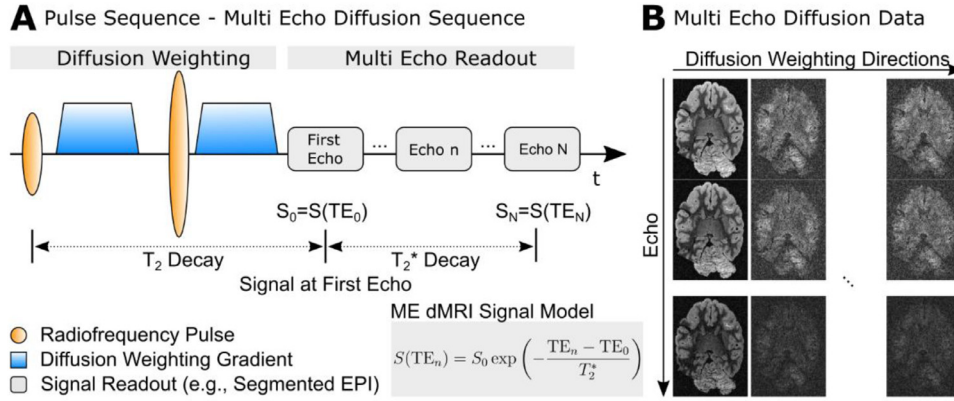
Fig. 1. Multi-Echo dMRI Acquisitions. (A) ME-dMRI acquisition employs a Stejskal-Tanner dMRI sequence, with a total acquisition of N gradient-echoes. ME-dMRI signals are described using a mixed decay model, where the first echo follows T_2 decay and the latter echoes follow T_2^* decay. (B) ME-dMRI data are multi-dimensional with N echo times and multiple diffusion directions.

noise, thereby preventing accurate signal averaging and modelling (Basu et al., 2006; Eichner et al., 2015; Gudbjartsson and Patz, 1995).

Due to the time-consuming diffusion contrast encoding, dMRI data are typically acquired using Echo-Planar-Imaging (EPI). However, EPI based acquisitions are especially prone to image distortions from eddy currents or magnetic field inhomogeneities (Andersson and Sotiropoulos, 2016). A further general challenge of dMRI is its inefficient signal acquisition strategy, in which diffusion contrast encoding can be of longer duration than the imaging readout.

Multiple strategies have been suggested to counteract typical issues associated with dMRI acquisitions. The signal bias of low SNR data can be overcome using phase-correction of the complex-valued dMRI dataset (Eichner et al., 2015). High in-plane acceleration using parallel imaging EPI can typically reduce geometrical distortions (Eichner et al., 2014; Griswold et al., 2002; Hamilton et al., 2017; Heidemann et al., 2012; Pruessmann et al., 1999).

For *post-mortem* dMRI acquisitions, these *in-vivo* strategies are not sufficient to achieve acceptable image quality. Captured air bubbles induce strong susceptibility differences within the *post-mortem* sample, making the background phase hard to estimate. In addition, *post-mortem* brain containers shift the tissue-air boundary from multiple centimeters to a distance of just a few millimeters. These problems aggravate EPI distortions, even when using parallel imaging acceleration.

Segmented EPI (sEPI) acquisition strategies have been proposed to mitigate these problems and to achieve almost distortion-free EPI data - even under challenging *post-mortem* conditions. Similar to other parallel imaging techniques, sEPI only captures small portions of the total k-space for each EPI shot. Here, in contrast to parallel imaging, the missing k-space segments are acquired in separate sEPI shots. Segmented EPI allows much faster EPI readout than parallel imaging strategies, resulting in considerably reduced image distortion.. Segmented dMRI acquisitions can be achieved using interleaved segmentation along the phase encoding direction (Butts et al., 1994; McKinnon, 1993), or by segmentation of the readout direction (Porter and Heidemann, 2009). Due to gradient slew rate limitations, interleaved segmentation along the phase encoding direction can achieve higher acceleration than readout segmented acquisitions (Wang et al., 2018).

Similarly to dMRI, fMRI recordings may also suffer from low SNR conditions, which can result in artifacts and false-positive results for BOLD activation patterns (Poser and Norris, 2009; Speck and Hennig, 1998). In this context, Multi-Echo (ME) imaging combined with acquisition acceleration strategies were shown to improve the functional sensitivity by weighted echo summation or the estimation of tissue parameters (Kundu et al., 2013, Kundu et al., 2012; Poser et al., 2006).

Combinations of ME and dMRI strategies have previously been suggested to combine dMRI measurements with relaxometry (Chabert et al., 2014; Hutter et al., 2018) and reduce acquisition times of specific dMRI experiments (Baete and Boada, 2018; Franconi et al., 1997). The potential impacts of ME acquisitions on SNR and contrast have not been

evaluated in the context of diffusion-weighted MRI. In this context, short readout strategies such as sEPI can enable dense echo sampling of ME acquisitions and the combination of segmented with ME acquisitions might be especially beneficial.

In this work, we present a novel dMRI sequence for *post-mortem* acquisitions. Multiple gradient echoes of highly segmented EPI trains are acquired to achieve acquisitions with low distortions and minimal echo time. The resulting ME-dMRI signals are combined in an SNR optimal way without noise bias, using a T_2^* decay model and statistical modelling incorporating the underlying noise distribution. The developed acquisition strategy was employed to acquire high-resolution dMRI data of a *post-mortem* wild chimpanzee brain on a human-scale MRI system. An additional estimate of potential SNR benefit under *in-vivo* conditions is provided using numerical simulations.

2. Theory

2.1. Description of the sequence

The employed ME-dMRI sequence combines Stejskal-Tanner diffusion preparation (Stejskal and Tanner, 1965) with repetitions of N segmented EPI readouts at different echo times TE_n (Fig. 1A). The spin-echo condition is realized at the first echo time TE_0. Therefore, the signal intensity of $S_0 = S(TE_0)$ follows a T_2 decay[1] whereas the subsequent multiple gradient-echoes decay with T_2^*[2] (Fig. 1B). The signal envelope of ME-dMRI data as a function of TE_n, the echo time of the nth echo, is then given by

$$S\left(TE_n\right) = \underbrace{\tilde{S}_0 \exp\left(-\frac{TE_0}{T_2}\right)}_{S_0} \exp\left(-\frac{TE_n - TE_0}{T_2^*}\right) \tag{1}$$

Here, $\widetilde{S_0}$ describes the diffusion-weighted signal without the T_2 decay component. Since this study mainly focuses on improving the SNR by acquiring multiple gradient-echoes, the ME-dMRI signal decay will be considered with respect to the spin-echo signal S_0:

$$S\left(TE_n\right) = S_0 \exp\left(-\frac{TE_n - TE_0}{T_2^*}\right) = S_0 \exp\left(-\frac{\Delta TE_n}{T_2^*}\right) \tag{2}$$

2.2. Increasing signal to noise using multi-echo acquisitions

ME-dMRI acquisitions provide additional data from multiple echoes which can be employed to increase the SNR. Here, we estimate the SNR

---

[1] Human T_2 3T: *in-vivo* ~ 80–110 ms (Wansapura et al., 1999), *post-mortem* typically shorter (Blamire et al., 1999; Shatil et al., 2018)

[2] Human T_2^* 3T *in-vivo* ~ 41–63 ms (Kleban et al., 2020; Wansapura et al., 1999) , *post-mortem* typically shorter

gain from a ME-dMRI signal combination using the Linear Least Squares (LLS) regression formulation.

We will employ two assumptions: (i) The underlying T_2^* is known and will not be estimated from the ME-dMRI data. (ii) The measurement noise, ϵ, is assumed to follow a zero-mean Gaussian distribution with a standard deviation, σ. The measured signal, M, is described with Eq. (3):

$$M\left(\text{TE}_n\right) = S_0 \exp\left(-\frac{\Delta\text{TE}_n}{T_2^*}\right) + \epsilon \text{ with } \epsilon \sim N\left(0, \sigma^2\right) \tag{3}$$

Since T_2^* is known, $\exp(-\Delta\text{TE}_n/T_2^*)$, is a constant for each ΔTE_n. To estimate S_0, we normalize each $M(\text{TE}_n)$ with this constant. It becomes apparent that the relative error of S_0 estimations grows with TE. The error distribution is given by:

$$\epsilon_{\text{TE}_n} = \epsilon \, \exp\left(\frac{\Delta\text{TE}_n}{T_2^*}\right) \sim N\left(0, \left(\sigma \exp\left(\frac{\Delta\text{TE}_n}{T_2^*}\right)\right)^2\right) \tag{4}$$

Due to the increasing error, the overall benefit of using multiple gradient-echoes will depend on the parameters ΔTE, T_2^*, and the number of acquired echoes. If late echoes with strong error contamination are employed, the accuracy of the S_0 estimation will decrease compared to early echoes. Under the assumption of Gaussian noise, S_0 can be estimated as $\bar{S}_0$ using LLS regression on multiple echoes.

$$\overline{S}_0 = arg\min_{S_0} \frac{1}{N} \sum_n \left(M\left(\text{TE}_n\right) \exp\left(\frac{\Delta\text{TE}_n}{T_2^*}\right) - S_0\right)^2 \tag{5}$$

The LLS function is convex and has a unique solution with inverse or Moore-Penrose pseudoinverse estimation of S_0.

$$\overline{S}_0 = \frac{1}{N} \sum_n M\left(\Delta\text{TE}_n\right) \exp\left(\frac{\Delta\text{TE}_n}{T_2^*}\right) \equiv S_0 + \frac{1}{N} \sum_n \epsilon_{\text{TE}_n} \tag{6}$$

The S_0 estimate from the LLS regression of ME data with Gaussian noise follows a Gaussian distribution centred around S_0.

$$\bar{S}_0 \sim N\left(S_0, \underbrace{\left(\frac{\sigma}{N}\right)^2 \sum_n \left(\exp\frac{\Delta\text{TE}_n}{T_2^*}\right)^2}_{\sigma_{\text{ME}}^2}\right) \tag{7}$$

The standard deviation, σ_{ME}, of this $\bar{S}_0$ distribution leads to an analytical expression of SNR gain from ME signal estimation using LLS on Gaussian distributed data, G_{SNR}.

$$G_{\text{SNR}} = \frac{N}{\sqrt{\sum_n \left(\exp\frac{\Delta\text{TE}_n}{T_2^*}\right)^2}} \tag{8}$$

From Eq. (8) it is concluded that, the SNR gain is a function of both tissue T_2^* and echo sampling scheme. For the limiting case of $T_2^* \to inf$, G_{SNR} converges towards $\sqrt{N}$, which equals the error reduction obtained by N averages (i.e. echoes). This represents the theoretical maximum SNR gain for ME-dMRI acquisitions underlying a given sampling scheme. Another limiting case of Eq. (8) emerges when the echo spacing of the individual echo acquisitions is minimized (i.e., $\Delta\text{TE}_n \to 0$), e.g., by employing stronger segmentation. Here, in a similar fashion, G_{SNR} also converges towards $\sqrt{N}$, regardless of the underlying T_2^* decay.

An analysis of Eq. (8) reveals $\sqrt{N}$ to be the limiting optimal case of ME reconstruction. For less asymptotic cases (i.e., $T_2^* << inf$, or $\Delta\text{TE}_n > 0$) more advanced model fitting strategies such as non-linear and weighted optimization might further increase the SNR gain from using ME-dMRI data.

Eq. (8) also shows, that for each TE sampling scheme and T_2^*, there is an optimal number of echoes, N, which can be used to increase G_{SNR}.

Due to the exponential decay of the dMRI signal, additional acquisitions of further echoes after this sweet spot will not anymore contribute to an SNR increase. A tool to numerically identify the optimal number of echoes for a given protocol will be made available online.[3]

2.3. Sensitivity and snr gain using statistical data modelling

The assumption of zero-mean Gaussian noise generally does not hold for diffusion-weighted MRI, where low SNR values induce a signal bias. Therefore, for unbiased estimates of S_0, it is beneficial to employ more advanced model fitting approaches, incorporating the nature of the underlying noise distribution.

In contrast to LLS, the Maximum Likelihood Estimation (MLE) achieves parameter estimations of models given specific data distributions (Thompson, 1963). By maximizing the likelihood function, MLE finds the most probable parameters of a function S to describe a given set of measurement data. MLE proves especially useful for non-Gaussian data distributions, such as dMRI data. For optimal coil combinations in complex space, dMRI signals follow a Rician data distribution characterized by the standard deviation of the underlying complex-valued noise, σ_C. Using MLE, model parameters of S, under a Rician data distribution, are computed by maximizing the logarithm of the likelihood function, L (Sijbers et al., 1998):

$$\log L \sim \sum_n \log I_0\left(\frac{S_n M_n}{\sigma_C^2}\right) - \sum_n \frac{S_n^2}{2\sigma_C^2} \tag{9}$$

In this equation, I_0 refers to the zeroth order modified Bessel function of the first kind, M_n refers to the nth echo of the measured data and S_n refers to the nth echo of the approximated signal function. In contrast to LLS, MLE enables unbiased estimations of model parameters by including a noise distribution model into the parameter estimation (Karlsen et al., 1999; Sijbers and Den Dekker, 2004). MLE has been shown to provide highly efficient approximations of the data by approaching the Cramér–Rao lower bound for parameter estimations (Karlsen et al., 1999). Noise informed reconstructions have previously been suggested to improve accuracy of relaxometry measurements (e.g., El Hajj et al., 2019; Hedström et al., 2017), as well as diffusion model fits (e.g., Wegmann et al., 2017).

Due to the non-linear weighted nature of MLE, an analytical SNR gain evaluation becomes nontrivial. We, therefore, employed numerical methods to assess the benefits of MLE parameter estimation.

3. Methods

To evaluate the benefit of using Multi-Echo dMRI acquisitions, we implemented a ME-dMRI sEPI sequence and acquired data from a *post-mortem* chimpanzee brain. We performed numerical simulations on synthetic ME-dMRI with matching acquisition parameters to compute the SNR gain as well as potential biases from reconstructions.

3.1. Numerical simulations of signal reconstruction

Monte Carlo simulations of ME reconstructions were employed to numerically assess reconstruction accuracy for low signals and the SNR benefit from ME-dMRI, using both LLS and MLE reconstructions. To ensure comparability with the acquired ME-dMRI chimpanzee data, simulations were performed on synthetic data with a similar ME sampling scheme (i.e., numbers of echoes, echo times).

3.1.1. Evaluation of the reconstruction bias

Diffusion-weighted MRI acquisitions typically suffer from low SNR - especially in the main direction of diffusion attenuation, where diffusion contrast is strongest. To preserve the diffusion contrast, it is crucial that

---

[3] Code available on https://github.com/cornelius-eichner

ME reconstructions retain an unbiased estimation of S_0, especially for small signals. Synthetic ME-dMRI data with $T_2^* = 30$ ms (white matter, see results) were generated, at five equidistantly spaced echo times from $\Delta TE = 0$ ms to $\Delta TE = 23.6$ ms. The choice of ΔTE reflects the echo distance, which was achievable in the *post-mortem* acquisition. Three sets of ME data were concatenated to mimic a ME-dMRI acquisition with three repetitions. The signal decay curves with $S_0 = 1$ were corrupted with complex noise. Both the real and magnitude part of the data were extracted to generate both Gaussian and Rician distributed data. Noise corrupted datasets were generated for 100 equidistantly spaced σ_{Noise}, with $\sigma_{Noise,max} = 1$ to $\sigma_{Noise,min} = 0.01$, thereby creating decay curves at 100 different SNR levels ($SNR_{min} = 1$, $SNR_{max} = 100$). Please note that the SNR level is only valid for the first echo time, as the signal intensity decays for later echoes. LLS and MLE reconstructions of both Gaussian and Rician distributed data were performed for 1000 repetitions of each SNR level.

3.1.2. Computation of SNR gain

The analytical assessment of SNR gain from ME-dMRI data acquisitions shows a dependency of G_{SNR} on the ME sampling scheme and the underlying T_2^* (Eq. (8)). To numerically probe this relation for LLS and MLE reconstructions, we created synthetic ME data for 100 equidistantly spaced T_2^* values ranging from $T_2^*{}_{min} = 1$ ms to $T_2^*{}_{max} = 100$ ms. Synthetic data were generated at five equidistantly spaced echo times from $\Delta TE = 0$ ms to $\Delta TE = 23.6$ ms. Signal decay curves were corrupted with both Gaussian and Rician noise. The SNR of the noisy data was set to $SNR = 5$ at the first echo time. LLS and MLE reconstructions were performed for 1000 repetitions for each T_2^* value. Reconstructions using LLS regression were performed non iteratively using Eq. (6). Reconstructions using MLE regression were performed by maximizing the log-likelihood of the signal (LLS for Gaussian noise and Eq. (9) for Rician data) using the Broyden-Fletcher-Goldfarb-Shanno (BFGS) algorithm (Byrd et al., 1995) as implemented in Python-SciPy (Virtanen et al., 2020).

For each T_2^* value, the SNR gain G_{SNR} was computed as the ratio of the standard deviation of a single echo, σ_{Noise}, to σ_{S_0} - the standard deviation obtainable from the fitting of multiple echoes.

$$G_{SNR} = \frac{\sigma_{Noise}}{\sigma_{S_0}} \tag{10}$$

In order to employ the numerically obtained MLE SNR gains (Eq. (10)) to experimental T_2^* data, they were globally smoothed using a Savitzky-Golay filter and subsequently interpolated using cubic polynomials, as implemented in Python-SciPy. The SNR gain map was calculated by applying this interpolation function on the pre-calculated T_2^* map.

3.1.3. In-vivo *SNR gain*

SNR gains of ME-dMRI for *in-vivo* acquisitions were estimated using Eq. (8) in conjunction with typical *in-vivo* scan parameters. In this context, the duration of the EPI train was calculated from assumed sequence parameters, to characterize the TE sampling scheme. The following sequence parameters were chosen: $N = 3$, $TE = 80$ ms, Matrix Size PE = 128, Echo Spacing = 0.6 ms, In Plane Acceleration Factor = 2, Partial Fourier = 6/8. Calculations were performed for moderate (Segmentation Factor = 2) and strong segmentation (Segmentation Factor = 4) along the PE direction. The sequence parameters resulted in an echo sampling $\Delta TE = [0, 14.4, 28.8]$ ms for moderate segmentation and $\Delta TE = [0, 7.2, 14.4]$ ms for strong segmentation. The G_{SNR} calculations were based on the T_2^* of three white matter tissues at 3T: Corpus Callosum: $T_2^*{}_{CC} = 58.5$ ms, Cingulum: $T_2^*{}_{Cing} = 50.3$ ms, Corticospinal Tract: $T_2^*{}_{CST} = 53.3$ ms (Kleban et al., 2020).

3.2. Data acquisition

3.2.1. Specimen

MRI data were acquired from the brain of a 6-year-old juvenile wild female chimpanzee from Taï National Park, Côte d'Ivoire (Wittig, 2018). The animal died from natural causes without human interference. The brain was extracted on-site by a veterinarian and immersion-fixed with 4% paraformaldehyde with a very short *post-mortem* interval of only 4 h. The performing veterinarian was specifically trained in field primate brain extractions, wearing full Personal Protective Equipment, and strictly adhering to the necropsy protocols of the field site. The procedures followed the ethical guidelines of primatological research at the Max Planck Institute for Evolutionary Anthropology, Leipzig, which were approved by the ethics committee of the Max Planck Society. The specimen was transferred to Germany strictly following CITES protocol regulations. After fixation for 6 months, the superficial blood vessels were removed, the formaldehyde was washed out in phosphate-buffered saline (PBS) pH 7.4 for 24 days. Subsequently, the brain was placed for scanning in an egg-shaped acrylic container filled with perfluoropolyether (PFPE, Solvay Solexis, Bollate, Italy). To prevent potential leakage of PFPE during the acquisition, the container was vacuum sealed using commercially available synthetic foil packaging (Caso Design, Arnsberg, Germany).

3.2.2. MR data acquisition

A Stejskal-Tanner diffusion-weighted MRI sequence (Stejskal and Tanner, 1965) was implemented to enable segmented EPI acquisitions of multiple echoes on a human clinical MRI system (see Fig. 1A). Diffusion-weighted MRI data of the *post-mortem* specimen were acquired at 3T on a MAGNETOM Skyra Connectom MRI system (Siemens Healthineers, Erlangen, Germany) using a maximum gradient strength of $G_{Max} = 300$ mT/m with a slew rate of 200T/m/s and a 32 channel phased-array coil (Siemens Healthineers, Erlangen) with the following imaging parameters: 0.8 mm nominal isotropic resolution, FoV = 128×96 mm^2, TR = 6105 ms, TE = [45.0, 50.9, 56.8, 62.7, 68.6] ms, 40 segments in phase encoding direction, BW = 976 Hz/Px, Adaptive-Combine coil-combination (Walsh et al., 2000), no partial Fourier, no parallel acceleration, whole-brain coverage with 80 slices. The choice of five echoes was based on an analysis of Eq. (8), using the provided tool, assuming a T_2^* of 30 ms for white matter.

The ME-dMRI acquisition time was extended by approximately 30% compared to a Single-Echo (SE) acquisition with otherwise identical parameters. Segmented EPI echo time-shifting was employed to minimize phase-discrepancies between segments (Feinberg and Oshio, 1994).

Three repetitions of 60 diffusion-weighted volumes ($b = 5000$ s/mm^2) alongside with 7 interspersed b0 images per repetition were acquired. In a prior assessment with multiple b-values, this diffusion weighting resulted in the highest diffusion contrast. Due to fixation related effects of the *post-mortem* tissue, a typically considered large diffusion weighting of $b = 5000$ s/mm^2 generated an average signal attenuation of only $\sim 70\%$ (equivalent to *in-vivo* $b = 1500$ s/mm^2, assuming white matter mean diffusivity MD = 0.84×10^{-3} mm^2/s as in Uddin et al., 2019).

To reduce potential impacts of magnetic field drift resulting from lengthy *post-mortem* dMRI acquisitions, the acquisition was split into multiple ~ 1 h scans with prior frequency adjustment.

To minimize impacts from short term instabilities such as heating and tissue movement, 90 min of dummy scans were run prior to the actual data acquisition (Dyrby et al., 2011). Data from these dummy scans were discarded from all further analyses. The total acquisition time for the data acquisition was 13 h 40 *m* + 90 m preceding dummy scans. An evaluation of the gradient heating revealed that the temperature approached steady state already after few minutes. Therefore, such extended dummy scans were not necessary to bring this MRI system on operating temperature.
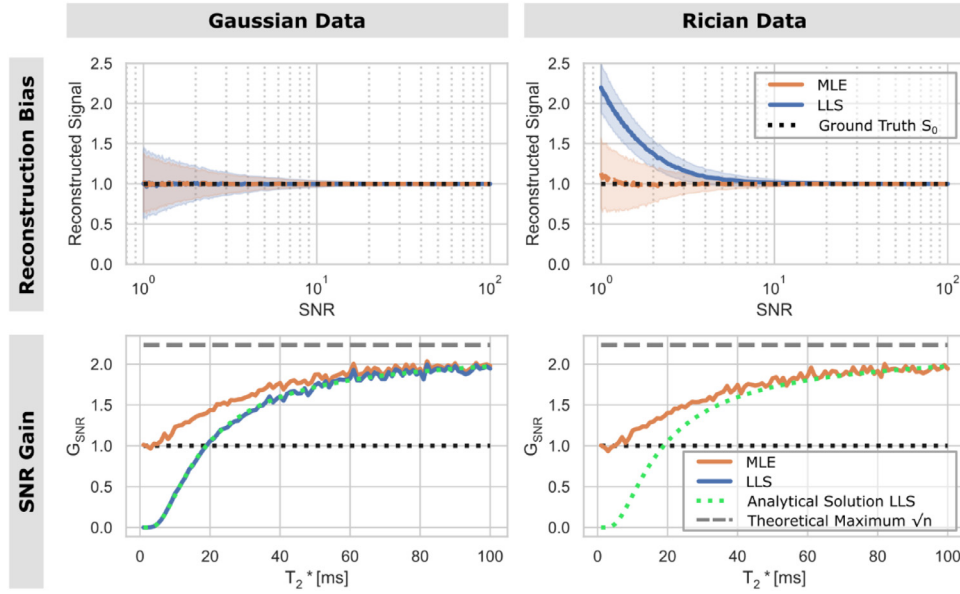
Fig. 2. Monte Carlo Simulation Results for ME Reconstructions using MLE and LLS Regression. Top Left: Reconstructed $S_0 = 1$ for 1000 repetitions for multiple Gaussian SNR levels (Log Scale). Shaded areas of the curve show standard deviations across the simulation population. No signal bias is induced, even for very low SNR levels. Bottom Left: SNR Gain for LLS and MLE ME-dMRI reconstructions for Gaussian data at various T_2^* decays. Monte Carlo simulations of the LLS reconstruction display high agreement with the analytical derivation of SNR gain. MLE reconstruction achieves higher SNR gain, especially at lower T_2^* values. Top Right: Reconstructed $S_0 = 1$ for 1000 repetitions for multiple Rician SNR levels. LLS reconstruction bias occurs for SNR≤10 and increases with decreasing SNR values. MLE performs an accurate estimation of S_0 up to SNR = 1. Bottom Right: SNR Gain MLE ME-dMRI reconstructions on Rician data. MLE reconstruction achieves comparable SNR gain as for Gaussian data MLE across the entire range of T_2^*.

For a statistical characterization of Rician noise of the dMRI acquisition, a noise map was recorded with identical parameters as the ME-dMRI sequence but without signal excitation (0.8 mm nominal isotropic resolution, FoV = 128×96 mm$^2 \times 80$ sl, TR = 6105 ms, TE = 45.0 ms, 40 segments in phase encoding direction, BW = 976 Hz/Px, Adaptive-Combine coil-combination, no partial Fourier, no parallel acceleration).

A 3D ME-FLASH sequence with 22 echoes was acquired for an accurate calculation of quantitative T_2^* with high SNR: 0.7 mm nominal isotropic resolution, FoV = $112 \times 100.1 \times 98$ mm^3, TR = 50 ms, TE = 2.2 - 42.5 ms, $\theta = 32°$

3.2.3. ME-dMRI reconstruction

The ME FLASH data were employed to calculate a whole-brain quantitative T_2^* map. In this context, the data were fit voxel-wise to an exponential T_2^* decay model using SciPy *curve fit* (Virtanen et al., 2020). The model parameters were enforced to be positive. ME-dMRI S_0 was reconstructed voxel-wise, using both LLS (Eq. (6)) and MLE regression (Eq. (9)). Here, all three repetitions of ME-dMRI data were jointly employed for the estimation of S_0. The quantitative T_2^* map was registered to the ME-dMRI data and included as a ground truth estimation for both LLS and MLE reconstructions. This enabled voxel-wise S_0 calculation for ME-dMRI using the T_2^* map. MLE reconstruction of Rician data requires a standard deviation estimate of the underlying complex noise, σ_C. The whole-brain noise distribution was characterized using the acquired noise map, using a recently published method to describe multi-coil data (St-Jean et al., 2020). Due to the employed Adaptive-Combine coil-combination in complex space, the magnitude dMRI data approximate a Rician data distribution (Sakaie and Lowe, 2017). Hence, Eq. (9) is applicable for computations of S_0. MLE reconstruction was performed similarly to the preceding simulations, using BFGS optimization.

4. Results

4.1. Numerical simulations of signal reconstructions

4.1.1. ME reconstruction accuracy

The Monte Carlo simulation results on reconstruction accuracy are summarized in Fig. 2 (top). For Gaussian distributed data, both LLS and MLE reconstruction achieve an accurate and unbiased reconstruction of the signal $S_0 = 1$ over the full range of simulated SNR values. For Rician distributed data the LLS reconstructions of data with SNR≤10 resulted in an overestimation of S_0. The simulations show that the overestima-

tion of S_0 for Rician data increases steadily with decreasing SNR values. This fact is particularly problematic for the reconstruction of dMRI data, where diffusion contrast is provided through signal attenuation. MLE reconstructions did not show overestimations of S_0 at low(er) SNR values and allowed an unbiased ME reconstruction of S_0 values down to SNR = 1. For Rician data, only a slight signal overestimation by approx. 10% becomes visible at SNR = 1.

Monte Carlo simulations suggest that employing MLE in ME-dMRI reconstructions is favourable due to its ability to deal with low SNR values of S_0.

4.1.2. SNR gain

Fig. 2 (bottom) summarizes the SNR gain, depending on the underlying T_2^* decay. Under the assumption of Gaussian noise, the results precisely follow the analytical prediction of SNR gain from Eq. (8). For growing T_2^* values, the SNR gain of ME-dMRI asymptotically approaches the theoretical maximum SNR gain by using 5 acquisitions (i.e., echoes), $\sqrt{5}$. When more echoes are recorded, the theoretical maximum SNR gain will also increase. For the LLS reconstruction of ME data, the employed sampling scheme did not automatically result in an increase in SNR. Both the simulations and the analytical prediction reveal an SNR gain with LLS only for T_2^* values above 20 ms. This shortcoming of LLS reconstruction can be explained by the error term, increasing error with TE$_n$ (Eq. (4)) - for short T_2^* values the error of later echoes (ε_{TE}) is too high to achieve an SNR gain. ME-dMRI acquisition do not benefit from later echoes in a similar fashion as ME-fMRI approaches since, in contrast to fMRI (Posse et al., 1999), the diffusion contrast does not evolve with increasing TE. Therefore, it is crucial to minimize the echo dependent error term by means of fast and dense sampling of early echoes.

MLE shows a different behavior of SNR gain across the simulated T_2^* range for both the Gaussian and Rician data distributions. In both cases, SNR loss was not observed - even for short T_2^* values. Instead, the SNR gain converges to $G_{SNR} = 1$ for small T_2^* values, where neither SNR gain nor loss will occur. Furthermore, MLE reconstruction achieves a greater SNR gain than LLS over the entire range of simulated T_2^* values. MLE on Gaussian data reduces to a least-squares problem, which is similar to the LLS algorithm. Therefore, the SNR gain compared to the LLS computation from Eq. (6) might be attributed to the employed non-linear BFGS optimization algorithm. The key advantage of MLE optimization is the ability to achieve SNR gains > 1 over the whole T_2^* range, especially for Rician distributed data.

Table 1
SNR Gain Factor Calculations for In-Vivo Acquisitions. The additional SNR benefit of using ME-dMRI also for *in-vivo* acquisitions depends on the applied sampling scheme and the underlying tissue T_2^*.

WM Tissue	Segmentation	EPI Readout Duration [ms]	G_{SNR}	Eq. Avg
CC	2	14.4	1.30	1.69
	4	7.20	1.52	2.30
Cingulum	2	14.4	1.23	1.52
	4	7.20	1.48	2.19
CST	2	14.4	1.26	1.59
	4	7.20	1.50	2.24

In summary, MLE reconstruction enables accurate and unbiased reconstructions of S_0 with high SNR. Monte Carlo simulations suggest that MLE is an optimal reconstruction method for reconstructing ME-dMRI data.

4.1.3. In-vivo SNR gain

The G_{SNR} results under simulated *in-vivo* conditions are summarized in Table 1. The provided results indicate, that G_{SNR} depends on both tissue T_2^* and TE sampling scheme. The average G_{SNR} gain across white matter tissues for moderate segmentation factors was $G_{SNR} = 1.26$, equivalent to 1.60 averages. For stronger in-plane segmentation factors, the SNR gain increased to $G_{SNR} = 1.5$, equivalent to 2.25 averages. The acquisition of additional echoes increased the total acquisition time by a factor of only 1.38 and is therefore more temporally efficient than additional averaging.

The current estimates were calculated assuming non iterative LLS echo combination. Given the previous simulation results, the SNR gain is expected to be larger for MLE using nonlinear optimization schemes.

4.2. ME-dMRI reconstruction

Fig. 3A compares reconstruction results from Single-Echo and Multi-Echo dMRI acquisitions. The raw data quality of the first echo is shown in the top row. The SNR gain of the acquired ME-dMRI data (three repetitions, five echoes) becomes visible in comparison with the SE-dMRI data (three repetitions, single echo). When comparing ME-dMRI reconstructions, it is apparent that the diffusion attenuation contrast is considerably more pronounced for MLE reconstructions. Hence, the ME-dMRI reconstruction results support the previous simulation results by demonstrating that MLE regression prevents signal bias for small S_0 values.

Fig. 3B shows the signal intensity histogram for MLE and LLS ME-dMRI reconstructions. Noise-induced bias becomes visible when comparing the signal distributions across the whole-brain volume for both diffusion-weighted and non-diffusion-weighted volumes. Here, LLS reconstructions show a tendency towards increased image intensities - i.e., a weakening of the diffusion contrast compared to MLE.

4.3. SNR gain map

Fig. 4 displays the whole-brain T_2^* map as well the associated SNR gain from using ME-dMRI alongside with MLE reconstruction. Given a specific ME sampling scheme the voxel-specific SNR is defined by the underlying T_2^* map (Fig. 4A). The quantitative T_2^* measurements show a distribution, ranging from ~ 20 ms to ~ 80 ms across the brain (Fig. 4B). The numerically generated SNR gain for this T_2^* distribution using MLE is summarized in Fig. 4C. The SNR gain from a single repetition of ME-dMRI shows a tissue-specific SNR gain of ~ 1.6 (WM, equivalent to 2.6 averages) and ~ 1.9 (GM, equivalent to 3.6 averages). From the G_{SNR} histogram in Fig. 4D, it is apparent that different tissue types generate distinct SNR gains. Inclusions of air bubbles can reduce T_2^* within a small radius as a result of susceptibility differences. In such areas, the Multi-Echo combination does not allow significant SNR gain, as T_2^* is too short. Please note that these results are shown for a single Multi-Echo

combination. Experimentally, a total of three repetitions were recorded, increasing the final SNR by an additional factor of $\sqrt{3}$.

5. Discussion

In dMRI acquisitions, accurate and unbiased measurements of signal attenuation are key to reconstruct fiber orientations or diffusion models with sufficient accuracy. Diffusion-weighted MRI measurements are based on selective signal attenuation and consequently suffer from intrinsically low SNR. In advanced dMRI, spatial resolution and diffusion-weighting are continuously increased (Haldar et al., 2016; Setsompop et al., 2018; Veraart et al., 2019). Such measurements more accurately capture the structure of the brain and allow better characterizations of underlying tissue microstructure. However, low SNR regimes are a limiting factor in such advanced dMRI acquisitions, thereby dampening the diffusion contrast and accurate model estimations from such measurements.

Here we present a novel strategy to increase SNR and reduce the signal bias from non-Gaussian noise for advanced dMRI acquisitions with low SNR. In this context, we developed a diffusion-weighted sEPI sequence capable of recording Multi-Echo signals following each diffusion preparation period. The Multi-Echo data are reconstructed using a signal relaxation model and a quantitative T_2^* map. The additionally required T_2^* map can be recorded within a few minutes - a time effort disproportionate to typically time-consuming *post-mortem* dMRI measurements.

To ensure accurate and optimal reconstructions of ME-dMRI data, we performed numerical Monte-Carlo simulations of different reconstruction algorithms and data types across various signal parameters. The simulations demonstrated optimal SNR gain and minimal signal bias using Maximum Likelihood Estimation reconstruction incorporating the Rician distribution of the data. Both simulations and analytical evaluation of the optimization problem showed an SNR gain dependency on both underlying T_2^* and the Multi-Echo sampling density. In our case, the SNR gain of white matter was 1.6 - which is equivalent to 2.6 averages. For grey matter, the SNR gain was 1.9 - equivalent to 3.6 averages. The SNR gain of up to 3.6 averages comes at the cost of an only slightly extended measurement time of approximately 30%. Using these 30% to acquire additional data (e.g., diffusion directions) would only contribute to a moderate SNR increase of $G_{SNR} = \sqrt{1.3} \sim 1.14$.
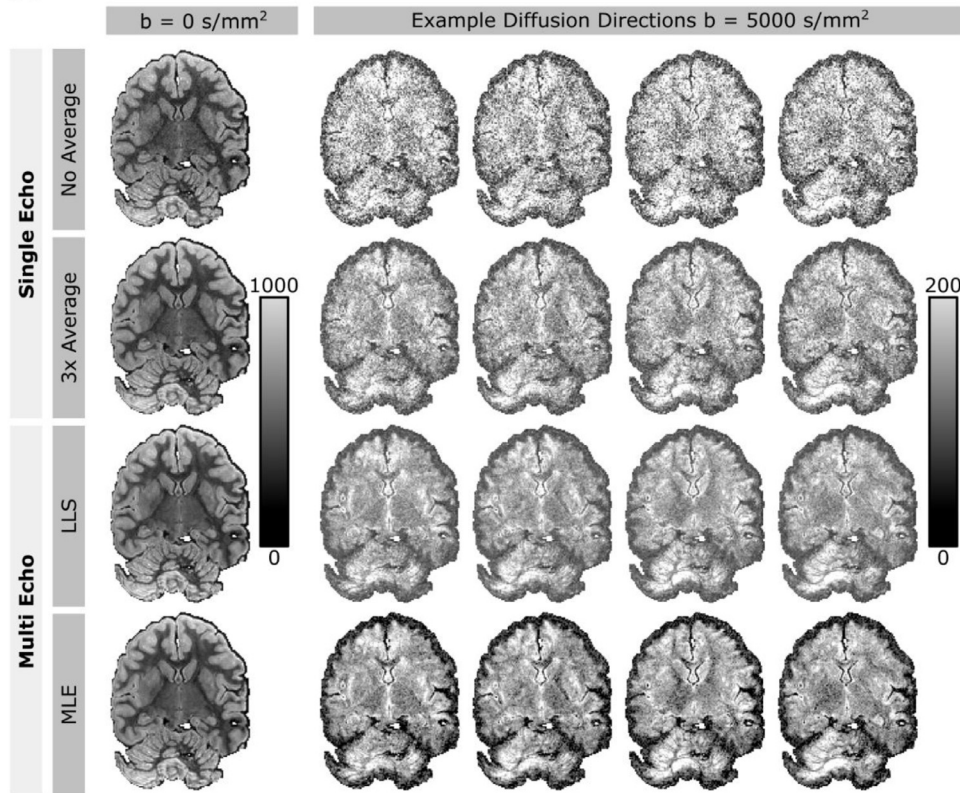
The second advantage of ME reconstructions using MLE is the low signal bias. Since MLE can incorporate the underlying noise distribution into the S_0 computation, the reconstructed signal remains unbiased, even for very low SNR levels of SNR ~ 1. An LLS reconstruction of the same data led to signal bias already present at SNR = 10. Therefore, MLE allows an unbiased reconstruction of the ME-dMRI data of signals with attenuations of almost an additional order of magnitude. This is particularly important in diffusion imaging, where low signals must be calculated with maximum precision. Simulations showed that ME-dMRI is very stable towards deviations in the T_2^* estimations (e.g., due to diffusion weighting, see supplementary material)

To put our proposed method to direct use, we recorded *post-mortem* dMRI data of a wild chimpanzee brain with high resolution and strong diffusion-weighting. The reconstruction of the acquired ME-dMRI data resulted in high-quality results with a noticeable SNR gain. In addition, the ME-dMRI reconstructions are in agreement with the simulations such that the desired diffusion contrast strongly increased when MLE reconstruction was used.

The implementation of this sequence on a human-scale MRI system capable of a maximum gradient strength of 300 mT/m allowed the acquisition of dMRI data with high diffusion-weightings to study the connectivity of whole brains up to human size. Thereby, sufficient directional diffusion contrast was achieved in *post-mortem* tissue, which requires stronger b-values to achieve similar contrast compared to *in-vivo* tissue.

The high spatial resolution of the acquired dMRI data provides the basis for a more accurate reconstruction of the white matter tracts com-

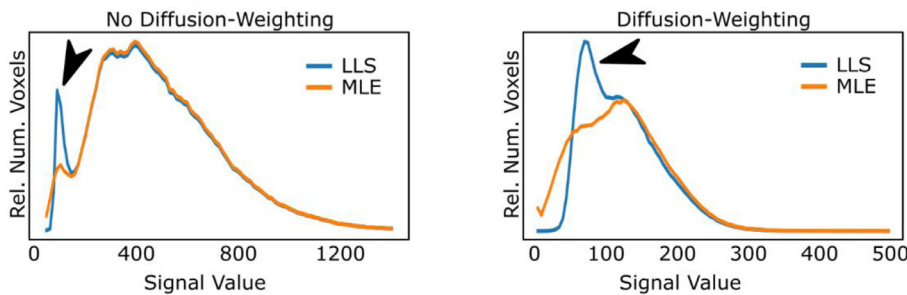**A** Single-Echo and Multi-Echo dMRI Reconstructions

Fig. 3. Exemplary Single-Echo and Multi Echo Reconstructions for B0 and Exemplary Diffusion Directions. (A) Single-Echo: The non-averaged Single-Echo diffusion-weighted data display very poor SNR (top row). Threefold averaging of dMRI data introduces improvements of image SNR scaled by $\sqrt{3}$ (second row). Multi Echo: Multi Echo dMRI acquisitions displays clearly visible SNR benefits. When comparing LLS (row three) and MLE reconstructions (row four), the benefits of noise informed MLE reconstructions become evident. MLE reconstructions display a much stronger diffusion contrast due to a better reconstruction of diffusion signal attenuation. (B) Distributions of reconstructed ME-dMRI data show differences, only for low signal intensities in both dMRI data without (left) and with diffusion-weighting (right).

B Distributions of Signal Values Multi-Echo dMRI Reconstructions

pared to typical *in-vivo* scans. This reduces the potential pitfalls of diffusion MRI tractography (Jones et al., 2013) and allows reconstructing the endpoints of the fiber pathways with greater precision.

The use of sEPI acquisitions allows minimizing image distortions which are caused by susceptibility differences. This enables more precise measurements of anatomical structures and is most relevant for *post-mortem* acquisitions, which may include captured air bubbles and strong susceptibility contrasts at the edges of the brain container.

When going to acquisitions at higher field strengths, ME-dMRI data might lose SNR gain due to potentially arising through-slice-dephasing. Here, locally reduced T_2^* across a slice might result in faster signal decay and, hence reduced G_{SNR}. The use of SSFP sequences or multiple spin echoes instead of gradient-echoes might help mitigating this problem, but would introduce additional challenges, such as less exact definitions of diffusion weighting or additional RF energy deposition. Within the framework of ME-dMRI, through slice dephasing effects could be mitigated by using (i) strong readout segmentations to quickly sample echoes, (ii) thinner slices or (iii) slab-based acquisitions.

The discussed ME approach is not limited to *post-mortem* dMRI sEPI acquisitions. The concept of ME-dMRI could also be used to increase the SNR and reduce signal bias in other settings. Segmented EPI dMRI acquisitions might also be acquired *in-vivo*, utilizing phase-navigators (Holdsworth et al., 2008; Porter and Heidemann, 2009) or advanced reconstruction mechanisms (Chen et al., 2013; Mani et al., 2016). *In-vivo* acquisitions especially benefit from a substantially prolonged T_2^*, making ME-dMRI SNR gains also feasible with typically employed segmentation factors. In this work, simulations of *in-vivo* acquisitions showed that ME-dMRI can achieve $G_{SNR} = 1.26$ (equivalent to 1.60 averages) or $G_{SNR} = 1.5$ (equivalent to 2.25 averages) within white matter, depending on the in-plane acceleration. These results indicate that *in-vivo* applications of ME-dMRI data might also be beneficial. Future research will explore the implementation of ME-dMRI to become available also *in-vivo*.

Even though a 300 mT/m gradient system was employed in this work, the achievable SNR gain does not depend on the underlying MRI gradient strength. The maximum gradient strength only affects the first
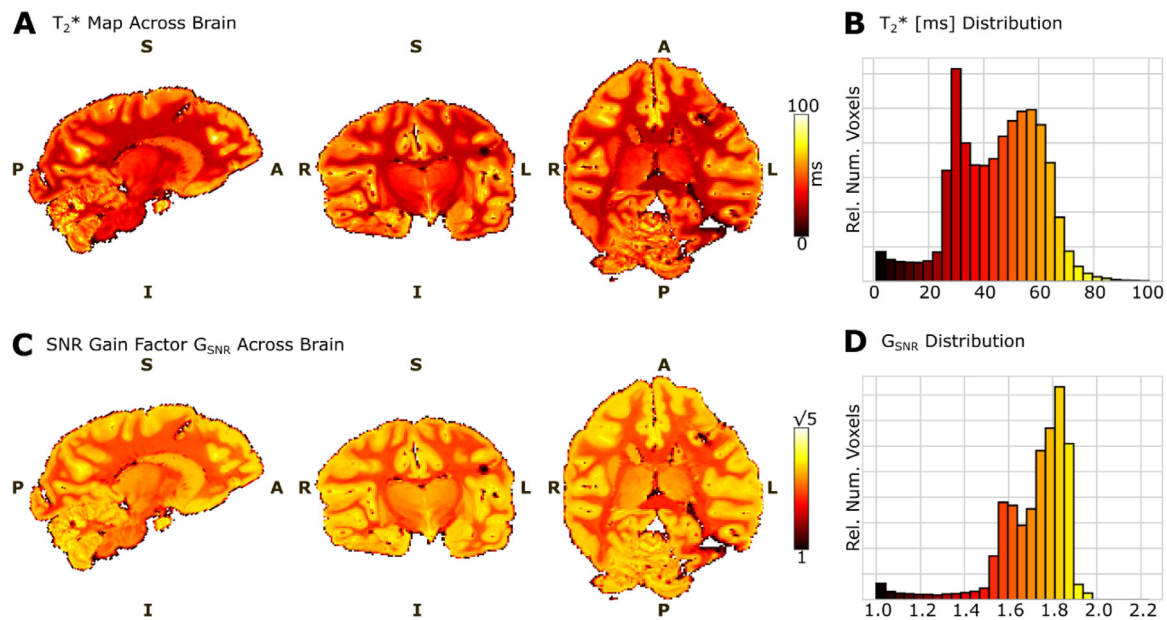
Fig. 4. T_2^*-dependent SNR Gain of ME-dMRI Acquisitions. (A) Whole-brain T_2^* map in orthographic view. (B) The T_2^* histogram displays a bimodal T_2^* distribution across the brain with WM $T_2^* \sim 30$ ms and GM $T_2^* \sim 60$ ms. Voxels with very low T_2^* values (< 25 ms) are likely caused by residual air bubbles. (C) Whole-brain map of T_2^* dependent SNR gain. G_{SNR} of ME-dMRI is strongest in areas of long T_2^*, such as in GM. The SNR gain map is windowed to the theoretical SNR gain of $\sqrt{5}$ from acquired 5 acquisitions (echoes). (D) Histograms of SNR gain from one repetition of ME-dMRI show a tissue-dependent SNR gain of ~ 1.6 (WM, equivalent to 2.6 averages) and ~ 1.9 (GM, equivalent to 3.6 averages). The SNR gain was calculated using the results from the Monte Carlo simulations. The whole-brain SNR gain increases if shorter readout trains enable higher density sampling of the first echoes.

echo by the length of the diffusion encoding time, but not the echo sampling rate. ME-dMRI acquisitions can be used on a wide range of MRI systems, ranging from clinical to preclinical MRIs. If ME-dMRI is employed in conjunction with sEPI, head gradient systems would allow for faster TE sampling due to increased gradient slew rates.

ME-dMRI acquisition schemes are not exclusively applicable by using sEPI. Instead, they can be extended to non-EPI based acquisition strategies. In the potential use of ME-dMRI with single line sequences, which represent the highest possible segmentation, the SNR increase could be even larger due to a denser sampling of early echoes. Also, additional research should investigate whether ME-dMRI can be beneficially combined with otherwise orthogonal *post-mortem* acquisition strategies such as DW SSFP (McNab and Miller, 2010).

This work predominantly focused on using ME-dMRI acquisitions to increase the image SNR. An alternative option to utilize ME-dMRI data would be to relate macroscopic T_2^* decays with the applied diffusion weighting. Such combinations of diffusion weighting and relaxometry can provide additional tissue information to gain better understanding of the underlying microstructure (Hutter et al., 2018). However, it should be noted that estimations of additional parameters from the same ME-dMRI data would also reduce the achievable SNR gain.

The concept of noise informed decay modelling is applicable to all MRI modalities where non-Gaussian noise can induce signal biases. Noise informed MLE fitting can be beneficial for the quantitative mapping of magnetic tissue properties. For example, noise informed MLE reconstruction could be advantageous for other quantitative MRI strategies using Multi-Echo acquisitions such as ME-FLASH (Helms et al., 2008) or ME-MP2RAGE (Metere et al., 2017). Multi-Echo reconstructions are commonly performed using LLS (Tabelow et al., 2019; Weiskopf et al., 2014). Especially at high resolutions or for *post-mortem* acquisitions, signal bias effects may be circumvented using advanced regression strategies such as MLE. We expect advanced fitting strategies to also be beneficial to diffusion relaxometry, where signal attenuation is generated not only from diffusion-weighting but also

from additional mechanisms such as T_1 relaxation and T_2 relaxation (Hutter et al., 2018; Slator et al., 2019; Tax et al., 2019).

6. Conclusion

Here we present Multi-Echo dMRI - a new concept to both increase image SNR and simultaneously reduce signal-biases of noise-corrupted dMRI data for *post-mortem* acquisitions. Diffusion MRI acquisitions typically suffer from a low temporal encoding efficiency, where a time-consuming contrast encoding is followed by a rather rapid acquisition of only one signal. Through the rapid sequential recording of multiple echoes, this new acquisition and reconstruction strategy makes better use of the diffusion-weighted signal and results in a more time-efficient contrast encoding. The presented ME-dMRI technique might also be beneficial to *in-vivo* dMRI acquisitions as well as quantitative relaxometry.

CRediT authorship contribution statement

Cornelius Eichner: Conceptualization, Methodology, Software, Formal analysis, Investigation, Writing - original draft, Writing - review & editing, Visualization. **Michael Paquette:** Conceptualization, Methodology, Software, Formal analysis, Writing - original draft, Writing - review & editing. **Toralf Mildner:** Conceptualization, Software, Writing - original draft, Writing - review & editing. **Torsten Schlumm:** Conceptualization, Software, Data curation. **Kamilla Pléh:** Investigation, Resources, Writing - original draft. **Liran Samuni:** Investigation, Resources. **Catherine Crockford:** Investigation, Resources, Project administration, Funding acquisition. **Roman M. Wittig:** Investigation, Resources, Writing - original draft, Project administration, Funding acquisition. **Carsten Jäger:** Investigation, Resources, Writing - review & editing. **Harald E. Möller:** Conceptualization, Methodology, Writing - original draft, Writing - review & editing. **Angela D. Friederici:** Investigation, Resources, Writing - original draft, Project administration, Supervision, Funding acquisition. **Alfred Anwander:** Conceptualization,

References

Andersson, J.L.R., Sotiropoulos, S.N., 2016. An integrated approach to correction for off-resonance effects and subject movement in diffusion MR imaging. Neuroimage 125, 1063–1078. https://doi.org/10.1016/j.neuroimage.2015.10.019.

Baete, S.H., Boada, F.E., 2018. Accelerated radial diffusion spectrum imaging using a multi-echo stimulated echo diffusion sequence. Magn. Reson. Med. 79 (1), 306–316. https://doi.org/10.1002/mrm.26682.

Basu, S., Fletcher, T., Whitaker, R., 2006. Rician noise removal in diffusion tensor MRI. Med. Image Comput. Comput. Assist. Interv. 9 (Pt 1), 117–125. https://doi.org/10.1007/11866565_15.

Blamire, A.M., Rowe, J.G., Styles, P., McDonald, B., 1999. Optimising imaging parameters for Post Mortem MR imaging of the human brain. Acta radiol. 40 (6), 593–597. https://doi.org/10.3109/02841859909175593.

Butts, K., Riederer, S.J., Ehman, R.L., Thompson, R.M., Jack, C.R., 1994. Interleaved echo planar imaging on a standard MRI system. Magn. Reson. Med. 31 (1), 67–72. https://doi.org/10.1002/mrm.1910310111.

Byrd, R.H., Lu, P., Nocedal, J., Zhu, C., 1995. A Limited Memory Algorithm for Bound Constrained Optimization. SIAM J. Sci. Comput. 16 (5), 1190–1208. https://doi.org/10.1137/0916069.

Chabert, S., Galindo, C., Tejos, C., Uribe, S.A., 2014. Multiple echo multi-shot diffusion sequence. J. Magn. Reson. Imaging. 39 (4), 1027–1032. https://doi.org/10.1002/jmri.24244.

Chen, N.kuei, Guidon, A., Chang, H.C., Song, A.W., 2013. A robust multi-shot scan strategy for high-resolution diffusion weighted MRI enabled by multiplexed sensitivity-encoding (MUSE). Neuroimage 72, 41–47. https://doi.org/10.1016/j.neuroimage.2013.01.038.

Dyrby, T.B., Baaré, W.F.C., Alexander, D.C., Jelsing, J., Garde, E., Søgaard, L.V., 2011. An ex vivo imaging pipeline for producing high-quality and high-resolution diffusion-weighted imaging datasets. Hum. Brain Mapp. 32 (4), 544–563. https://doi.org/10.1002/hbm.21043.

Eichner, C., Cauley, S.F., Cohen-Adad, J., Möller, H.E., Turner, R., Setsompop, K., Wald, L.L., 2015. Real diffusion weighted MRI enabling true signal averaging and increased diffusion contrast. Neuroimage 122, 373–384. https://doi.org/10.1016/j.neuroimage.2015.07.074.

Eichner, C., Setsompop, K., Koopmans, P.J., Lützkendorf, R., Norris, D.G., Turner, R., Wald, L.L., Heidemann, R.M., 2014. Slice accelerated diffusion-weighted imaging at ultra-high field strength 4th ed. Magn. Reson. Med. 71, 1518–1525. https://doi.org/10.1002/mrm.24809.

El Hajj, C., Moussaoui, S., Collewet, G., Musse, M., 2019. Spatially regularized multi-exponential transverse relaxation times estimation from magnitude magnetic resonance images under rician noise. In: Proceedings - International Conference on Image Processing. ICIP.

Feinberg, D.A., Oshio, K., 1994. Phase errors in multi-shot echo planar imaging. Magn. Reson. Med. 32 (4), 535–539. https://doi.org/10.1002/mrm.1910320418.

Franconi, F., Lethimonnier, F., Sonier, C.B., Pourcelot, L., Akoka, S., 1997. Diffusion imaging with a multi-echo MISSTEC sequence. J. Magn. Reson. Imaging. 7 (2), 399–404. https://doi.org/10.1002/jmri.1880070225.

Griswold, M.A., Jakob, P.M., Heidemann, R.M., Nittka, M., Jellus, V., Wang, J., Kiefer, B., Haase, A., 2002. Generalized autocalibrating partially parallel acquisitions (GRAPPA). Magn. Reson. Med. 47 (6), 1202–1210. https://doi.org/10.1002/mrm.10171.

Gudbjartsson, H., Patz, S., 1995. The rician distribution of noisy mri data. Magn. Reson. Med. 34 (6), 910–914. https://doi.org/10.1002/mrm.1910340618.

Haldar, J.P., Fan, Q., Setsompop, K., 2016. Whole-brain quantitative diffusion MRI at 660μm resolution in 25 min using gSlider-SMS and SNR-enhancing joint reconstruction. Proc. Intl. Soc. Mag. Reson. Med. 0102.

Hamilton, J., Franson, D., Seiberlich, N., 2017. Recent advances in parallel imaging for MRI. Prog. Nucl. Magn. Reson. Spectrosc. 101, 71–95. https://doi.org/10.1016/j.pnmrs.2017.04.002.

Hedström, E., Voigt, T., Greil, G., Schaeffter, T., Nagel, E., 2017. Automatic T2* determination for quantification of iron load in heart and liver: a comparison between automatic inline Maximum Likelihood Estimate and the truncation and offset methods. Clin. Physiol. Funct. Imaging. 37 (3), 299–304. https://doi.org/10.1111/cpf.12303.

Heidemann, R.M., Anwander, A., Feiweier, T., Knösche, T.R., Turner, R., 2012. k-space and q-space: combining ultra-high spatial and angular resolution in diffusion imaging using ZOOPPA at 7T. Neuroimage 60, 967–978. https://doi.org/10.1016/j.neuroimage.2011.12.081.

Helms, G., Dathe, H., Dechent, P., 2008. Quantitative FLASH MRI at 3T using a rational approximation of the Ernst equation. Magn. Reson. Med. 59 (3), 667–672. https://doi.org/10.1002/mrm.21542.

Holdsworth, S.J., Skare, S., Newbould, R.D., Guzmann, R., Blevins, N.H., Bammer, R., 2008. Readout-segmented EPI for rapid high resolution diffusion imaging at 3T. Eur. J. Radiol. 65 (1), 36–46. https://doi.org/10.1016/j.ejrad.2007.09.016.

Hutter, J., Slator, P.J., Christiaens, D., Teixeira, R.P.A.G., Roberts, T., Jackson, L., Price, A.N., Malik, S., Hajnal, J.V., 2018. Integrated and efficient diffusion-relaxometry using ZEBRA. Sci. Rep. 8 (1), 15138. https://doi.org/10.1038/s41598-018-33463-2.

Jones, D.K., Alexander, D.C., Bowtell, R., Cercignani, M., Dell'Acqua, F., McHugh, D.J., Miller, K.L., Palombo, M., Parker, G.J.M., Rudrapatna, U.S., Tax, C.M.W., 2018. Microstructural imaging of the human brain with a 'super-scanner': 10 key advantages of ultra-strong gradients for diffusion MRI. Neuroimage. 182, 8–38. https://doi.org/10.1016/j.neuroimage.2018.05.047.

Jones, D.K., Knösche, T.R., Turner, R., 2013. White matter integrity, fiber count, and other fallacies: the do's and don'ts of diffusion MRI. Neuroimage 73, 239–254. https://doi.org/10.1016/j.neuroimage.2012.06.081.

Karlsen, O.T., Verhagen, R., Bovée, W.M.M.J., 1999. Parameter estimation from Rician-distributed data sets using a maximum likelihood estimator: application to T1 and perfusion measurements. Magn. Reson. Med. 41 (3), 614–623. https://doi.org/10.1002/(SICI)1522-2594(199903)41:3<614::AID-MRM26>3.0.CO;2-1.

Kleban, E., Tax, C.M.W., Rudrapatna, U.S., Jones, D.K., Bowtell, R., 2020. Strong diffusion gradients allow the separation of intra- and extra-axonal gradient-echo signals in the human brain. Neuroimage 217, 116793. https://doi.org/10.1016/j.neuroimage.2020.116793.

Kundu, P., Brenowitz, N.D., Voon, V., Worbe, Y., Vértes, P.E., Inati, S.J., Saad, Z.S., Bandettini, P.A., Bullmore, E.T., 2013. Integrated strategy for improving functional connectivity mapping using multiecho fMRI. Proc. Natl. Acad. Sci. U. S. A. 110 (40), 16187–16192. https://doi.org/10.1073/pnas.1301725110.

Kundu, P., Inati, S.J., Evans, J.W., Luh, W.-M., Bandettini, P.a, 2012. Differentiating BOLD and non-BOLD signals in fMRI time series using multi-echo EPI. Neuroimage 60 (3), 1759–1770. https://doi.org/10.1016/j.neuroimage.2011.12.028.

Mani, M., Magnotta, V., Kelley, D., Jacob, M., 2016. Comprehensive reconstruction of multi-shot multi-channel diffusion data using mussels. In: Proceedings of the Annual International Conference of the IEEE Engineering in Medicine and Biology Society. EMBS, pp. 1107–1110.

McKinnon, G., 1993. Ultrafast interleaved gradient-echo-planar imaging on a standard scanner. Magn. Reson. Med. 30 (5), 609–616. https://doi.org/10.1002/mrm.1910300512.

McNab, J.A., Edlow, B.L., Witzel, T., Huang, S.Y., Bhat, H., Heberlein, K., Feiweier, T., Liu, K., Keil, B., Cohen-Adad, J., Tisdall, M.D., Folkerth, R.D., Kinney, H.C., Wald, L.L., 2013. The human connectome project and beyond: initial applications of 300mT/m gradients. Neuroimage 80, 234–245. https://doi.org/10.1016/j.neuroimage.2013.05.074.

McNab, J.A., Miller, K.L., 2010. Steady-state diffusion-weighted imaging: theory, acquisition and analysis. NMR Biomed. 23 (7), 781–793. https://doi.org/10.1002/nbm.1509.

Metere, R., Kober, T., Möller, H.E., Schäfer, A., 2017. Simultaneous quantitative MRI mapping of T1, T2* and magnetic susceptibility with multi-echo MP2RAGE. PLoS ONE 12, e0169265. https://doi.org/10.1371/journal.pone.0169265.

Miller, K.L., Stagg, C.J., Douaud, G., Jbabdi, S., Smith, S.M., Behrens, T.E.J., Jenkinson, M., Chance, S.A., Esiri, M.M., Voets, N.L., Jenkinson, N., Aziz, T.Z., Turner, M.R., Johansen-Berg, H., McNab, J.A., 2011. Diffusion imaging of whole, post-mortem human brains on a clinical MRI scanner. Neuroimage 57 (1), 167–181. https://doi.org/10.1016/j.neuroimage.2011.03.070.

Porter, D.A., Heidemann, R.M., 2009. High resolution diffusion-weighted imaging using readout-segmented echo-planar imaging, parallel imaging and a two-dimensional navigator-based reacquisition. Magn. Reson. Med. 62 (2), 468–475. https://doi.org/10.1002/mrm.22024.

Poser, B.A., Norris, D.G., 2009. Investigating the benefits of multi-echo EPI for fMRI at 7 T. Neuroimage 45 (4), 1162–1172. https://doi.org/10.1016/j.neuroimage.2009.01.007.

Poser, B.A., Versluis, M.J., Hoogduin, J.M., Norris, D.G., 2006. BOLD contrast sensitivity enhancement and artifact reduction with multiecho EPI: parallel-acquired inhomogeneity-desensitized fMRI. Magn. Reson. Med. 55 (6), 1227–1235. https://doi.org/10.1002/mrm.20900.

Posse, S., Wiese, S., Gembris, D., Mathiak, K., Kessler, C., Grosse-Ruyken, M.L., Elghahwagi, B., Richards, T., Dager, S.R., Kiselev, V.G., 1999. Enhancement of BOLD-contrast sensitivity by single-shot multi-echo functional MR imaging. Magn. Reson. Med. 42 (1), 87–97. https://doi.org/10.1002/(SICI)1522-2594(199907)42:1<87::AID-MRM13>3.0.CO;2-O.

Pruessmann, K.P., Weiger, M., Scheidegger, M.B., Boesiger, P., 1999. SENSE: sensitivity encoding for fast MRI. Magn. Reson. Med. 42 (5), 952–962. https://doi.org/10.1002/(SICI)1522-2594(199911)42:5%3C952::AID-MRM16%3E3.0.CO;2-S.

Roebroeck, A., Miller, K.L., Aggarwal, M., 2019. Ex vivo diffusion MRI of the human brain: technical challenges and recent advances. NMR Biomed. 32 (4), e3941. https://doi.org/10.1002/nbm.3941.

Sakaie, K., Lowe, M., 2017. Retrospective correction of bias in diffusion tensor imaging arising from coil combination mode. Magn. Reson. Imaging 37, 203–208. https://doi.org/10.1016/j.mri.2016.12.004.

Setsompop, K., Fan, Q., Stockmann, J., Bilgic, B., Huang, S., Cauley, S.F., Nummenmaa, A., Wang, F., Rathi, Y., Witzel, T., Wald, L.L., 2018. High-resolution in vivo diffusion imaging of the human brain with generalized slice dithered enhanced resolution: simultaneous multislice (gSlider-SMS). Magn. Reson. Med. 79 (1), 141–151. https://doi.org/10.1002/mrm.26653.

Setsompop, K., Kimmlingen, R., Eberlein, E., Witzel, T., Cohen-Adad, J., McNab, J.A., Keil, B., Tisdall, M.D., Hoecht, P., Dietz, P., Cauley, S.F., Tountcheva, V., Matschl, V., Lenz, V.H., Heberlein, K., Potthast, A., Thein, H., Van Horn, J., Toga, A., Schmitt, F., Lehne, D., Rosen, B.R., Wedeen, V., Wald, L.L., 2013. Pushing the limits of in vivo diffusion MRI for the Human Connectome Project. Neuroimage 80, 220–233. https://doi.org/10.1016/j.neuroimage.2013.05.078.

Shatil, A.S., Uddin, M.N., Matsuda, K.M., Figley, C.R., 2018. Quantitative Ex Vivo MRI changes due to progressive formalin fixation in whole human brain specimens: longitudinal characterization of diffusion, relaxometry, and myelin water fraction measurements at 3T. Front. Med. 5. https://doi.org/10.3389/fmed.2018.00031.

Sijbers, J., Den Dekker, A.J., 2004. Maximum likelihood estimation of signal amplitude and noise variance from MR data. Magn. Reson. Med. 51 (3), 586–594. https://doi.org/10.1002/mrm.10728.

Sijbers, J., Den Dekker, A.J., Scheunders, P., Van Dyck, D., 1998. Maximum-likelihood estimation of rician distribution parameters. IEEE Trans. Med. Imaging 17, 357–361. https://doi.org/10.1109/42.712125.

Slator, P.J., Hutter, J., Palombo, M., Jackson, L.H., Ho, A., Panagiotaki, E., Chappell, L.C., Rutherford, M.A., Hajnal, J.V., Alexander, D.C., 2019. Combined diffusion-relaxometry MRI to identify dysfunction in the human placenta. Magn. Reson. Med. 82 (1), 95–106. https://doi.org/10.1002/mrm.27733.

Speck, O., Hennig, J., 1998. Functional imaging by I0- and T2*-parameter mapping using multi- image EPI. Magn. Reson. Med. 40 (2), 243–248. https://doi.org/10.1002/mrm.1910400210.

Stejskal, E.O., Tanner, J.E., 1965. Spin diffusion measurements: spin echoes in the presence of a time-dependent field gradient. J. Chem. Phys. 42 (1), 288–292. https://doi.org/10.1063/1.1695690.

St-Jean, S., De Luca, A., Tax, C.M.W., Viergever, M.A., Leemans, A., 2020. Automated characterization of noise distributions in diffusion MRI data. Med. Image. Anal. 65. https://doi.org/10.1016/j.media.2020.101758.

Tabelow, K., Balteau, E., Ashburner, J., Callaghan, M.F., Draganski, B., Helms, G., Kherif, F., Leutritz, T., Lutti, A., Phillips, C., Reimer, E., Ruthotto, L., Seif, M., Weiskopf, N., Ziegler, G., Mohammadi, S., 2019. hMRI – A toolbox for quantitative MRI in neuroscience and clinical research. Neuroimage 194, 191–210. https://doi.org/10.1016/j.neuroimage.2019.01.029.

Tax, C.M.W., Rudrapatna, U.S., Mueller, L., Jones, D.K., 2019. Characterizing diffusion of myelin water in the living human brain using ultra-strong gradients and spiral readout. In: Proceedings of the 27th Annual Meeting of the International Society for Magnetic Resonance in Medicine, p. 1115.

Thompson, W.A., 1963. Mathematical Statistics, Technometrics. John Wiley & Sons, Inc., Hoboken, NJ, USA https://doi.org/10.1080/00401706.1963.10490115.

Uddin, M.N., Figley, T.D., Solar, K.G., Shatil, A.S., Figley, C.R., 2019. Comparisons between multi-component myelin water fraction, T1w/T2w ratio, and diffusion tensor imaging measures in healthy human brain structures. Sci. Rep. 9 (1). https://doi.org/10.1038/s41598-019-39199-x.

Veraart, J., Fieremans, E., Novikov, D.S., 2019. On the scaling behavior of water diffusion in human brain white matter. Neuroimage 185, 379–387. https://doi.org/10.1016/j.neuroimage.2018.09.075.

Virtanen, P., Gommers, R., Oliphant, T.E., Haberland, M., Reddy, T., Cournapeau, D., Burovski, E., Peterson, P., Weckesser, W., Bright, J., van der Walt, S.J., Brett, M., Wilson, J., Millman, K.J., Mayorov, N., Nelson, A.R.J., Jones, E., Kern, R., Larson, E., Carey, C.J., Polat, İ., Feng, Y., Moore, E.W., VanderPlas, J., Laxalde, D., Perktold, J., Cimrman, R., Henriksen, I., Quintero, E.A., Harris, C.R., Archibald, A.M., Ribeiro, A.H., Pedregosa, F., van Mulbregt, P., Vijaykumar, A., Bardelli, A, Pietro, Rothberg, A., Hilboll, A., Kloeckner, A., Scopatz, A., Lee, A., Rokem, A., Woods, C.N., Fulton, C., Masson, C., Häggström, C., Fitzgerald, C., Nicholson, D.A., Hagen, D.R., Pasechnik, D.V., Olivetti, E., Martin, E., Wieser, E., Silva, F., Lenders, F., Wilhelm, F., Young, G., Price, G.A., Ingold, G.L., Allen, G.E., Lee, G.R., Audren, H., Probst, I., Dietrich, J.P., Silterra, J., Webber, J.T., Slavič, J., Nothman, J., Buchner, J., Kulick, J., Schönberger, J.L., de Miranda Cardoso, J.V., Reimer, J., Harrington, J., Rodríguez, J.L.C., Nunez-Iglesias, J., Kuczynski, J., Tritz, K., Thoma, M., Newville, M., Kümmerer, M., Bolingbroke, M., Tartre, M., Pak, M., Smith, N.J., Nowaczyk, N., Shebanov, N., Pavlyk, O., Brodtkorb, P.A., Lee, P., McGibbon, R.T., Feldbauer, R., Lewis, S., Tygier, S., Sievert, S., Vigna, S., Peterson, S., More, S., Pudlik, T., Oshima, T., Pingel, T.J., Robitaille, T.P., Spura, T., Jones, T.R., Cera, T., Leslie, T., Zito, T., Krauss, T., Upadhyay, U., Halchenko, Y.O., Vázquez-Baeza, Y., 2020. SciPy 1.0: fundamental algorithms for scientific computing in Python. Nat. Methods 17, 261–272. https://doi.org/10.1038/s41592-019-0686-2.

Walsh, D.O., Gmitro, A.F., Marcellin, M.W., 2000. Adaptive reconstruction of phased array MR imagery. Magn. Reson. Med. 43 (5), 682–690. https://doi.org/10.1002/(SICI)1522-2594(200005)43:5<682::AID-MRM10>3.0.CO;2-G.

Wang, Y., Ma, X., Zhang, Z., Dai, E., Jeong, H.K., Xie, B., Yuan, C., Guo, H., 2018. A comparison of readout segmented EPI and interleaved EPI in high-resolution diffusion weighted imaging. Magn. Reson. Imaging 47, 39–47. https://doi.org/10.1016/j.mri.2017.11.011.

Wansapura, J.P., Holland, S.K., Dunn, R.S., Ball, W.S., 1999. NMR relaxation times in the human brain at 3.0 tesla. J. Magn. Reson. 9 (4), 531–538. https://doi.org/10.1002/(SICI)1522-2586(199904)9:4%3C531::AID-JMRI4%3E3.0.CO;2-L.

Wegmann, B., Eklund, A., Villani, M., 2017. Bayesian Rician regression for neuroimaging. Front. Neurosci. 11. https://doi.org/10.3389/fnins.2017.00586.

Weiskopf, N., Callaghan, M.F., Josephs, O., Lutti, A., Mohammadi, S., 2014. Estimating the apparent transverse relaxation time (R2*) from images with different contrasts (ESTATICS) reduces motion artifacts. Front. Neurosci. 8. https://doi.org/10.3389/fnins.2014.00278.

Wittig, R.M., 2018. Taï Chimpanzees, in: Encyclopedia of Animal Cognition and Behavior. Springer International Publishing, Cham, pp. 1–7.